Science of Sintering, **54** (2022)387-399

https://doi.org/10.2298/SOS2204387S

UDK: 539.53; 621.926.087; 692.533.1

Powder Metallurgy and Hardness of the Al-10Mg Alloy Reinforced with Carbon Nanotubes

Juan José Sánchez-Cuevas[1], Gerardo Rosas[1], Oracio Navarro[2], Cecilia Mercado-Zúñiga[3], Luis A. Bretado-Aragón[4], Francisco J. Reynoso-Marín[4], Juan Zárate-Medina[1*)]

[1]Instituto de Investigación en Metalurgia y Materiales, Universidad Michoacana de San Nicolás de Hidalgo, Ciudad Universitaria, Francisco J. Mújica S/N, Colonia Felicitas del Rio, C.P. 58030, Morelia, Michoacán, México.
[2]Instituto de Investigaciones en Materiales, Universidad Nacional Autónoma de México, Unidad Morelia, Antigua carretera a Pátzcuaro No. 8701, Colonia Ex Hacienda de San José de la Huerta, C.P. 58190, Morelia, Michoacán, México.
[3]Tecnológico de Estudios Superiores de Coacalco, Avenida 16 de Septiembre No. 54, Colonia Cabecera Municipal, C.P. 55700, Coacalco de Berriozábal, México, México.
[4]Ingeniería en Nanotecnología, Universidad de La Ciénega del Estado de Michoacán de Ocampo, Avenida Universidad No. 3000, Colonia Lomas de la Universidad, C.P. 59103, Sahuayo, Michoacán, México.

Abstract:

In this work, the multi-walled carbon nanotubes (MWCNTs) were purified with an acid treatment and subsequently dispersed using ultrasound and a nonionic surfactant solution of ethoxylated lauric alcohol 7 moles of ethylene oxide (E7E). Then, carbon nanotubes (CNTs) were used as a reinforcement phase (0.4 wt.% and 0.8 wt.%) in the Al-10Mg alloy. The high-energy ball milling was employed for the nanocomposites processing, and the resulting powders consolidate by uniaxial pressure. Measurements of Vickers microhardness, nanohardness, displacement, and Young's modulus were carried out on the compacts. The samples were analyzed using scanning electron microscopy (SEM), X-ray diffraction (XRD), ultraviolet-visible spectroscopy (UV-Vis), Fourier-transform infrared spectroscopy (FT-IR), and Raman spectroscopy (RS). Good dispersion of MWCNTs was achieved using 0.5 mg/ml of the E7E surfactant. The CNTs were dispersed in the Al-10Mg matrix using 0.25 h of milling. After powders compaction, the Al-10Mg/0.4MWCNTs nanocomposite presented a microhardness of 190 HV, nanohardness of 3.5 GPa, and Young's modulus 116 GPa.

Keywords*: Al-10Mg/MWCNTs nanocomposites; High-energy ball milling; Microhardness; Nanohardness; Young's modulus.*

1. Introduction

Light structural materials such as Al, Mg, and their alloys have many applications in the automotive and aerospace industries, mainly due to their high strength/weight ratio, low density, ductility, corrosion resistance, good thermal and electrical conductivity [1-3]. However, these materials' low mechanical resistance limits their use [4]. Consequently, metal

*) **Corresponding author:** jzaratemedina@gmail.com; jzarate@umich.mx

matrix nanocomposite materials (MMCs) constituted by the physical mixture of phases have been developed. The MMCs properties depend on the individual materials and their distribution, volumetric fraction, interfacial interaction, and the preparation technique [5,6].
The reinforcement phase objective is to increase the matrix's mechanical characteristics, such as the maximum stress or the elasticity modulus. While the matrix's function is to maintain the shape, it keeps the fibers together and distributes the stresses [7,8].

The metal matrix's reinforcing materials can be ceramic particles or fibers that offer high mechanical strength and high modulus of elasticity, properties that make them optimal materials in various technological applications [9]. The most commonly reinforcement materials are, SiO_2 [10], Al_2O_3 [11], Y_2O_3 [12], ZrO_2 [13], TiC [14], B_4C [15], SiC [16], Si_3N_4 [17], graphene [18], fullerenes [19], and carbon nanotubes (CNTs) [20].

On the other hand, the discovery of CNTs has led to new materials with several potential applications since they have excellent mechanical, electrical, thermal, chemical, and optical properties [21,22]. Notably, the mechanical properties of CNTs such as stiffness, strength, resilience, and low density, make them good candidates as reinforcement materials in Al, Mg, Al-Mg, and other materials [23].

A uniform CNTs dispersion in metallic matrices has become the most critical challenge in MMCs given the Van der Waals and electrostatic forces that tend to its agglomeration, which plays a vital role achieving the theoretically predicted properties in various materials. Moreover, a good dispersion of CNTs is challenging to reach because of its high aspect ratio [24]. To overcome this disadvantage, more excellent dispersion and adherence methods require mechanical milling, ultrasound, magnetic stirring, and the modification of the surface energy of CNTs [25,26].

On the other hand, the synthesis of MMCs can be carried out by a wide variety of processing routes, among which we find; liquid metallurgy (stir casting) [27], and powder metallurgy (mechanical alloying (MA) and mechanical milling (MM)) [28]. The first is simple; however, there are difficulties in the dispersion and interaction of the CNTs with the matrix. Also, brittle aluminum carbide (Al_4C_3) is formed at high temperatures; this leads to a decrease in mechanical properties [29]. In contrast, MA is inexpensive and has reasonable control during processing.

Several investigations have concluded that MA is a valuable technique for the homogeneous dispersion of CNTs in the metal matrix [24,25,30]. However, MA provokes possible damage to CNTs, and mixing at the molecular level leads to an interface [24]. The last depends on optimizing the milling process conditions, for example, very long times generate contamination and molecular mixing, relatively short times can only cause slight damage to the nanostructures, but a good dispersion can be obtained. Furthermore, it is a suitable technique in which, in a single stage, a good homogenization in the metal matrix is achieved, in addition to the benefit of having a nanostructured alloy.

In the present work, we present the results of the microstructural and mechanical characterization of the Al-10Mg matrix reinforced with MWCNTs. The presence of Mg in Al decreases its ductility and increases resistance, given the lower stacking fault energy. The nanostructured Al-10Mg alloy obtained by MA increases the aluminum's mechanical resistance; it is also low weight and can be heat treated. The Al-10Mg alloy and nanocomposites' mechanical behavior was investigated by microhardness, nanohardness, and Young's modulus tests.

2. Materials and Experimental Procedures

The spray pyrolysis method synthesizes the MWCNTs from the catalytic decomposition of toluene and ferrocene at 850ºC for 40 min [31]. The toluene/ferrocene weight ratio was 96.5:3.5 (w/w). Ultra-high purity argon was used as stripping gas with a flow

rate of 2 l/min. A mixture of hydrochloric acid (HCl), nitric acid (HNO_3), and deionized water in a volumetric ratio of 1.0: 0.5: 1.0, respectively, purified the MWCNTs. The suspension was dispersed by ultrasound for 20 min and magnetically stirred (500 rpm) at 60ºC for 3 h. Then filtered and washed consecutively with deionized water until reaching a neutral pH. Finally, the MWCNTs were dried at 100ºC for 24 h.

The pre-dispersion consisted of preparing several colloidal suspensions of MWCNTs, for which it was necessary to add 1 mg to 7 ml of high purity isopropyl alcohol. Next, the nonionic surfactant ethoxylated lauric alcohol 7 moles of ethylene oxide (E7E) was added in different amounts (0.4, 0.5, 0.6, 0.7, 0.8, 0.9, 1, 2, 28 and 56 mg/ml) in order to observe which concentration presents the best dispersion. Finally, the suspensions were exposed to an ultrasound bath with a 42 kHz frequency for 1.5 h.

The Al-10Mg alloy was synthesized by high-energy mechanical milling from individual powders in previous work [32]. Briefly, the Al-10Mg alloy was prepared in a SPEX 8000M ball mill from elemental powders Al (granular < 1 mm) and Mg (chips, 4-30 mesh) with a purity of 99.70 wt.% and 99.98 wt.%, respectively. The process control agent was stearic acid (3 wt.%) and the milling time to obtain the alloy was 10 h.

The nanocomposites were manufactured using MWCNTs as reinforcement material (0.4 and 0.8 wt.%). The dispersion of the MWCNTs in the Al-10Mg matrix was carried out by ball milling in SPEX 8000M equipment at 1800 rpm, using a ball weight/powder weight ratio of 7:1. The vial and milling media were D2 type hardened stainless steel. Since the energy transferred during milling can damage or decrease the length of carbon nanostructures [33], was employed a short time of 0.25 h for the dispersion process. The subsequent stage consisted of the powders consolidation (Al-10Mg and Al-10Mg/MWCNTs) through uniaxial pressing using a preheating temperature of 300ºC and a pressure of 1500 MPa for 10 min. The Archimedes method calculates the density of the material. According to a previous study, a conventional oven was employed for the sintering process at 420ºC for 2 h [32]. The monoliths' microhardness evaluation was determined with a Mitutoyo model HM-200 Vickers indenter with a diamond tip, applying a load of 100 g for 15 s. The method developed by Oliver & Pharr [34,35] determines the nanohardness and Young's modulus by using the HYSITRON TI 700 Ubi nanoindenter with Berkovich-type geometry, applying a load of 2000 µN. The materials' morphological and structural characterization was performed by scanning electron microscopy (JEOL JSM-7600F), X-ray diffraction (Bruker D8 ADVANCE), using a stepwise of 1 s/0.02º. Raman spectroscopy was performed on Bruker Senterra equipment. Ultraviolet-visible spectroscopy using a Perkin Elmer Lambda 25 and finally, the Fourier transform infrared spectroscopy using a Bruker TENSOR 27 equipment.

3. Results and Discussion

3.1. Acid purification of MWCNTs

Fig. 1a-b shows two SEM micrographs taken at different magnifications (100X and 10000X) corresponding to the acid-purified MWCNTs. Because CNTs maintain the packet structure, they do not suffer significant damage having a length of approximately 500 µm and an external diameter between 42-100 nm. Linearity is related to the molecular structure of the carbon source [36]. Linear CNTs appear when hydrocarbons with a linear structure such as methane, ethylene, and acetylene are used. When cyclic hydrocarbons such as benzene, cyclohexane, and xylene are employed, CNTs curves are produced [37]. On the other hand, the acid route is carried out to reduce amorphous carbon and catalytic iron nanoparticles (FeNPs) significantly. The latter was corroborated by energy dispersive spectroscopy (EDS) chemical analysis, where the presence of iron was quantified, before and after purification, being 8.80 wt.% and 1.80 wt.%, respectively, which suggests an efficient route to reduce the Fe at about 80 wt.%.

Fig. 1c-d presents the X-ray diffractograms of the as-prepare and purified MWCNTs, respectively. The characteristic reflections of the MWCNTs (JCPDS no. 00-058-1638) are appreciated, denoting high crystallinity obtained after the purification process. Also, the diffraction peaks of graphite carbon (JCPDS no. 03-065-6212), iron impurities (JCPDS no. 99-101-0062), and magnetite formation (Fe_3O_4) (JCPDS no. 01-089-0950) appear. The low intensity of the impurities peaks with the purified treatment means a reduction in their presence, although they are still located inside the layers and the body of the MWCNTs.

Fig. 1e presents the Raman spectrum, where the D band located at 1347 cm^{-1} is distinguished, attributed to the crystalline defects in the walls of the CNTs. Besides, the G band located at 1578 cm^{-1} is related to graphitization and C-C vibration. Finally, the G' band situate at 2689 cm^{-1} is associated with the characteristic resonance of defects and disorders induced in the crystal lattice. The intensity ratio I_D/I_G was 0.24, while the ratio $I_{G'}/I_D$ was 3.17. When I_D/I_G has a low value accompanied by a high $I_{G'}/I_D$ value, a minimum of defects is denoted in CNTs [38].

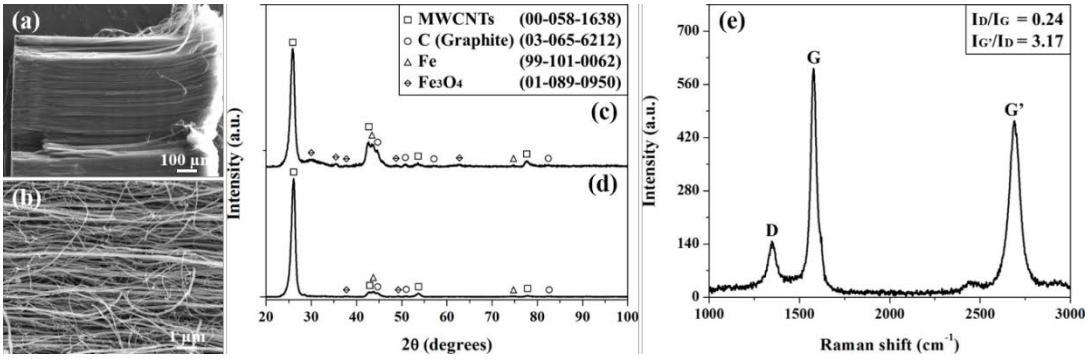

Fig. 1. Characterization of the MWCNTs by different techniques. SEM micrographs at a) 100X and b) 10000X magnifications. X-ray diffraction patterns of c) unpurified and d) purified, and e) Raman Spectrum of purified.

3.2. Dispersion of MWCNTs in E7E

Fig. 2a shows the UV-Vis spectra corresponding to the CNTs suspensions with and without surfactant (black line). In the absence of the surface agent, good absorbance is not present, which indicates low dispersion. Besides, for low concentrations of surfactant, the absorbance increases, while it decreases at higher concentrations, implying a more significant effect of the surfactant for smaller amounts. These results are also corroborated by analyzing the digital photograph (insert), showing suspensions of CNTs with different surfactant concentrations, where at low values, the samples turn entirely dark, indicating high dispersion, being the best 0.5 mg/ml.

Fig. 2b-c present SEM images recorded at 10000X, corresponding to the suspensions of CNTs without and with a surfactant, respectively. Fig. 2b shows an ultrasonic scattering of the CNTs without surfactant, denoted by their random orientation. Suspension of the ultrasonic bath leads to rapid agglomeration attributed to Van der Waals forces. However, when employing a concentration of 0.5 mg/ml surfactant, the dispersion effect is noticeable, presenting an established physical bond between the surfactant monomers and the nanotubes' surface due to electrostatic repulsion between the polar heads of the surfactant (Fig. 2c).

Fig. 2d corresponds to the FT-IR spectrum after the purification step, in which the characteristic absorption bands occur. A band broad with medium intensity appears to wavenumber 3443 cm^{-1}, attributed to the tension vibration of the hydroxyl group (O-H), which is related to the formation of hydrogen, carboxyl (COOH), or adsorption of water on

the surface of the CNTs due to the purification treatment. The peaks located at 2922 cm^{-1} and 2853 cm^{-1} are related to the presence of functional groups of the methyl (CH_3) and methylene (CH_2) type, associated with structural defects in the nanotubes [39]. The absorption band at 1636 cm^{-1} is characteristic of the carbonyl group (C=O) tension vibration of the COOH molecule, while the band with weak intensity at 1433 cm^{-1} is associated with the tension vibration of the C-C. The peak appears at 1114 cm^{-1} is attributed to the tension vibration of the C-O group [38]. Finally, the bands at 875 cm^{-1} and 706 cm^{-1} are related to the Fe-O vibration of the magnetite phase (Fe_3O_4) [40,41]. Several active modes in the infrared can appear out of phase due to the nanotubes' geometry and diameter [42].

Fig. 2e shows the infrared spectrum of the nonionic surfactant E7E, where a band broad with low intensity appears at 3476 cm^{-1} attributed to O-H, present in the hydrophilic head of the surfactant. The peaks at 2922 cm^{-1} and 2854 cm^{-1} correspond to the CH_3 and CH_2 groups that form the hydrophobic chain. On the other hand, the absorbance in 1458 cm^{-1} is related to the C-H groups' presence, while the bands in the interval 1349-1102 cm^{-1} are characteristic of the C-O tension vibration. Finally, the peaks that appear in the range of 944-500 cm^{-1} are also characteristic of the C-H groups present in the surfactant's hydrophilic zone. Fig. 2f presents the FT-IR spectrum of the best dispersion obtained at 0.5 mg/ml. Characteristic absorptions of E7E appear in addition to the functional groups of the nanotubes. Besides, it is possible to notice a slight displacement and changes in the intensity of the bands. For example, the peak at 2922 cm^{-1} grows, while the band at 2854 cm^{-1} is suppressed, suggesting CH_3 groups present at the end of the hydrocarbon chain bind to the nanotube's surface, allowing the union of the hydrophobic zone. On the other hand, the bands present in the fingerprint region (1500-600 cm^{-1}) also showed changes in intensity attributed to adjacent interactions between monomers.

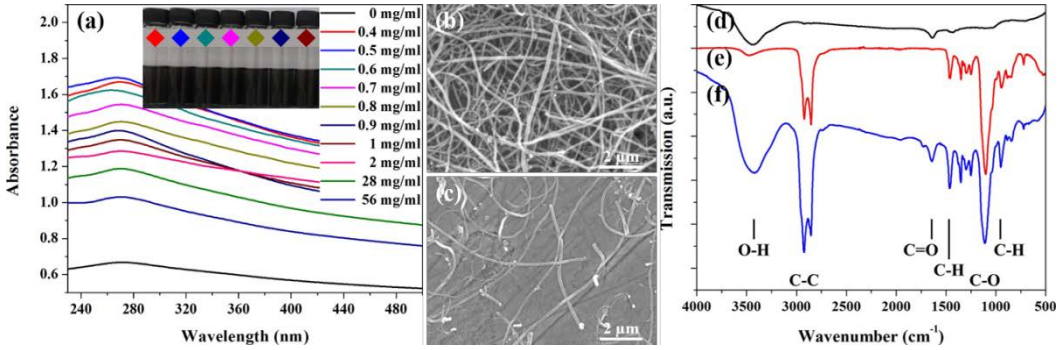

Fig. 2. Various characterization tecniques of dispersed MWCNTs. a) UV-Vis spectra at different surfactant concentrations, digital photograph expressing the best dispersion range, 0.4-1 mg/ml (insert). Micrographs at 10000X corresponding to the dispersions, b) without surfactant and c) with 0.5 mg/ml E7E. FT-IR spectra corresponding of d) purified, e) E7E surfactant, and f) dispersed with 0.5 mg/ml E7E.

3.3. Dispersion of MWCNTs in Al-10Mg by high-energy mechanical milling

Fig. 3a-b show SEM micrographs recorded at 10000X of the Al-10Mg powders reinforced with MWCNTs in 0.4 wt.% and 0.8 wt.%, respectively. These powders were dispersed by mechanical milling for 0.25 h. In both figures, CNTs appear homogeneously dispersed in the matrix. However, a decrease in the aspect ratio of CNTs occurs by decreasing from 500 µm to 2 µm. These results demonstrate the dispersion of CNTs in the matrix as a function of purification processes, ultrasound pre-dispersion, and high energy mechanical milling [43-45].

On the other hand, Fig. 3c shows the curve of densification *vs.* pressure corresponding to compacted powders. As the compaction pressure increased, the compacts' densification increased, being 89% for 1500 MPa. It is worth mentioning that at higher pressures up to 2000 MPa, the compact presents a separation between layers or laminations.

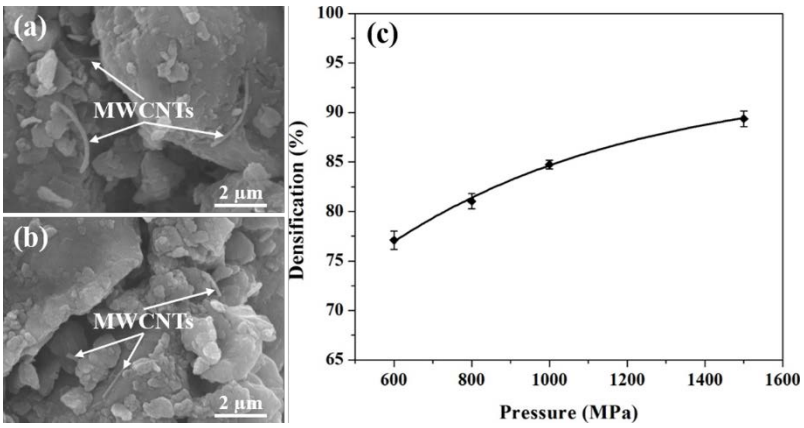

Fig. 3. SEM micrographs are corresponding to the nanocomposite powders. a) Al-10Mg/0.4MWCNTs, b) Al-10Mg/0.8MWCNTs, and c) densification curve *vs.* pressure corresponding to Al-10Mg with preheating to 300ºC and compacted at different pressures: 600, 800, 1000, and 1500 MPa.

3.4. Sintering of Al-10Mg alloy and Al-10Mg/MWCNTs nanocomposites

Fig. 4 shows several SEM micrographs with their respective EDS chemical composition spectrum. Each pair of items from top to bottom correspond to the samples Al-10Mg (a, a1), Al-10Mg/0.4MWCNTs (b, b1), and Al-10Mg/0.8MWCNTs (c, c1). The left column represents green compacted materials using preheating at 300 ºC for 3 min, while the right column shows the results after sintering at 420ºC for 2 h.

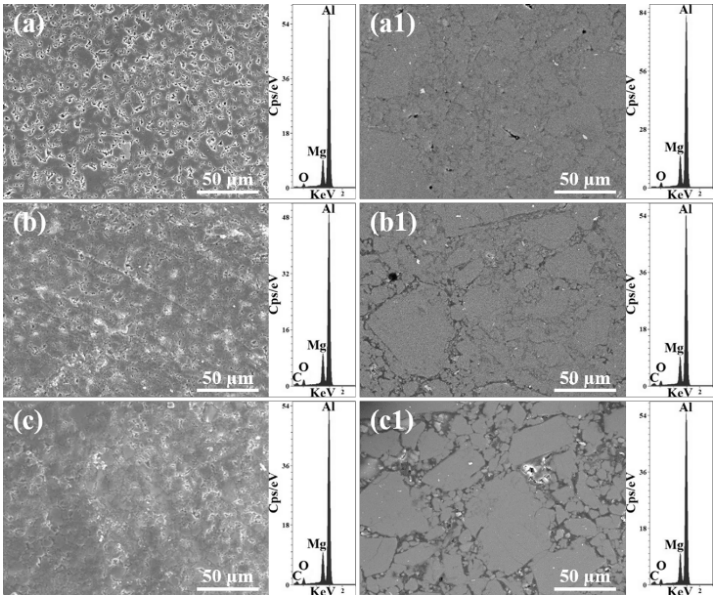

Fig. 4. SEM images (500X) of the samples Al-10Mg, Al-10Mg/0.4MWCNTs, and Al-10Mg/0.8MWCNTs in green (a, b, c) and sintered (a1, b1, c1).

After sintering, the particle size increases, while the porosity decreases, attributed to a greater diffusion of the elements, the compacts improve their densification values from 85 % to 91 %. It was reported that low particle growth accompanied by broad grain boundaries is related to the fixation of MWCNTs [46,47]. In the same figure, the EDS spectra show the chemical composition of the compacts. A slight increase in the O element after the sintering step indicates an oxide layer's formation that avoids particles diffuse, which prevents a better densification value.

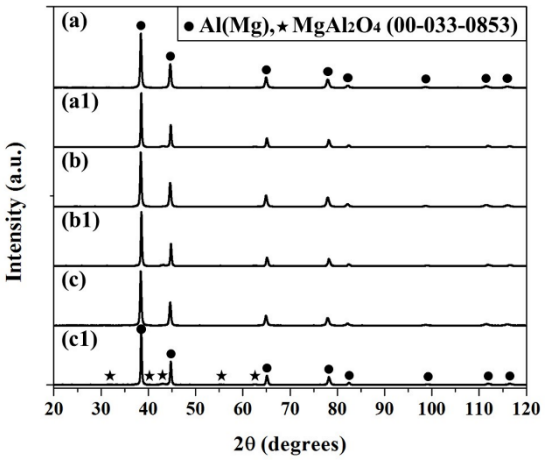

Fig. 5. X-ray diffraction patterns of the samples Al-10Mg, Al-10Mg/0.4MWCNTs, and Al-10Mg/0.8MWCNTs in green (a, b, c) and sintered (a1, b1, c1).

Fig. 5 shows the X-ray diffraction patterns corresponding to Al-10Mg, Al-10Mg/0.4MWCNTs, and Al-10Mg/0.8MWCNTs before (a, b, c) and after sintering (a1, b1, c1), respectively. XRD patterns before sintering show characteristic reflections of Al(Mg) fcc solid solution (JCPDS no. 00-004-0787). The XRD patterns after sintering display the $MgAl_2O_4$ spinel phase in addition to the Al(Mg) phase corresponding to JCPDS no. 00-033-0853. Table I presents the data of the structural analysis of the compacts. In the sintered samples, a slight decrease in the lattice parameter was determined, attributed to Mg segregation giving rise to the formation of $MgAl_2O_4$.

Tab. I Structural data and phase quantification, before and after sintering of Al-10Mg (a-a1), Al-10Mg/0.4MWCNTs (b-b1), and Al-10Mg/0.8MWCNTs (c-c1).

Material	**Experimental conditions T (ºC), t (h)**	**Lattice parameter (*a* = *b* = *c*) (Å)**	**Crystallite size (nm)**	**Al(Mg) (wt.%)**	**$MgAl_2O_4$ (wt.%)**
(a)	300, 0.05	4.07104 ± 0.00020	26.71 ± 0.64	100	-
(a1)	420, 2	4.06134 ± 0.00024	29.04 ± 2.51	97.46	2.54
(b)	300, 0.05	4.07104 ± 0.00020	26.71 ± 0.64	100	-
(b1)	420, 2	4.06163 ± 0.00034	30.15 ± 2.57	97.15	2.85
(c)	300, 0.05	4.07104 ± 0.00020	26.71 ± 0.64	100	-
(c1)	420, 2	4.06193 ± 0.00044	31.26 ± 2.63	96.85	3.15

As the amount of MWCNTs in the compound increased from 0.4-0.8 wt.%, the proportion of $MgAl_2O_4$ increased (≈ 3 wt.%). The $MgAl_2O_4$ presence could be beneficial in the system by increasing the matrix mechanical resistance. This result may be related to the functional groups (OH and COOH) adsorbed on the material. Sintering decomposes these groups and the surfactant due to its low boiling points, leading to the material's consequent oxidation.

Unlike other studies, the intermetallic γ-$Al_{12}Mg_{17}$, β-Al_3Mg_2 [48,49], and the compound Al_4C_3 [50] were not identified attributed to the formation of the spinel whose thermodynamics is more favorable. Other authors have studied the oxidation of this type of alloy and confirm the formation of $MgAl_2O_4$ [48]. Notably, the absence of a controlled atmosphere influences the oxidation of the Al-10Mg alloy. However, as mentioned in the previous paragraph, the greater oxidation can come from the functional groups that increase the reinforcement.

3.5. Vickers Microhardness tests

Fig. 6a-c present the optical micrographs of the Vickers microhardness indentation marks performed in Al-10Mg, Al-10Mg/0.4MWCNTs, and Al-10Mg/0.8MWCNTs after sintering, respectively. Fig. 6d shows the graph of the Vickers microhardness values along with porosity %. The Al-10Mg alloy presented an average value of microhardness of 150 HV. This data is higher than Al and Mg (45 HV and 46 HV, respectively) [51-54], attributed to the existence of nanocrystals and the presence of $MgAl_2O_4$.

Regarding the Al-10Mg/0.4MWCNTs nanocomposite profile indentation, a decrease in the mark's length can be observed concerning the previous one, indicating an increase in the hardness value (190 HV) achieved by the influence of MWCNTs; this value is higher than that reported in other investigations [52-56]. Finally, for the compound Al-10Mg/0.8MWCNTs, the hardness decreased with the previous sample, 171 HV. This decrease can be associated with an increase in porosity in the sample. For example, Fig. 6d presents the estimated porosity values for the materials; Al-10Mg (9 %), Al-10Mg/0.4MWCNTs (9.1%) and Al-10Mg/0.8MWCNTs (15%). The last value was 6 % higher than in the previous cases, related to the greater presence of $MgAl_2O_4$ determined by XRD, which prevents a good sintering process. As mentioned above, the higher percentage of reinforcement leads to a higher presence of surfactant, which could be influencing the oxidation of the material during sintering.

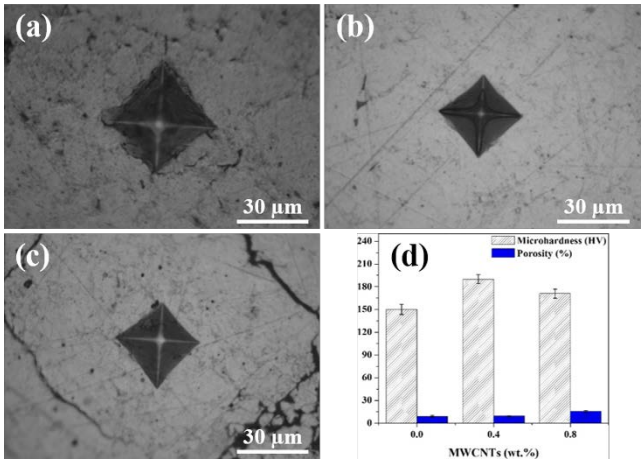

Fig. 6. Optical microscopy images belonging to the indentation traces made after sintering, (a) Al-10Mg, (b) Al-10Mg/0.4MWCNTs, and (c) Al-10Mg/0.8MWCNTs.

3.6. Nanohardness and Young's modulus

To further investigate the reinforcement of the Al-10Mg metal matrix, nanohardness measurements were carried out. Fig. 7a shows the load *vs.* displacement corresponding to indentations made in Al-10Mg, Al-10Mg/0.4MWCNTs, and Al-10Mg/0.8MWCNTs after sintering. The Al-10Mg matrix shows the most significant displacement of the graph, taken as

a reference value for the compounds. The nanocomposite with 0.4 wt.% CNTs display a smaller displacement, which indicates an increase in the resistance achieved by the presence of CNTs. However, for 0.8 wt.% CNTs, the shift increases concerning the addition of 0.4 wt.% CNTs, indicating a lower strength, which is related to the high porosity determined. These results agree very well with the Vickers microhardness test (see Fig. 6).

Fig. 7b shows the results of nanohardness and Young's modulus, which illustrates an improvement in the alloy's hardness with 0.4 wt.%, showing a value of 3.5 GPa. The nanohardness is reduced to 2.8 GPa for 0.8 wt.%. In any case, the last two results are superior to the matrix, which showed an average hardness of 2.4 GPa. These measurements affect Young's modulus values, being 116 GPa in 0.4 wt.%, 57 GPa in 0.8 wt.%, and 40 GPa in Al-10Mg. As can be seen, these values are influenced by the percentage of reinforcement and the distribution of CNTs. The good dispersion of these nanostructures resulted in charge transfer, which led to an increase in the nanocomposites' stiffness.

Consequently, the homogeneous dispersion of the MWCNTs caused an increase in microhardness, nanohardness, and Young's modulus, linked to the best interfacial interaction in the alloy. The latter may be related to the presence of $MgAl_2O_4$, since it can promote a more significant interaction of MWCNTs with the matrix due to the covalent bond between CNTs and $MgAl_2O_4$. These results are consistent with those obtained by other authors regarding the existence of oxides that can improve the interaction of CNTs, resulting in a benefit of the compound's mechanical properties [53,57].

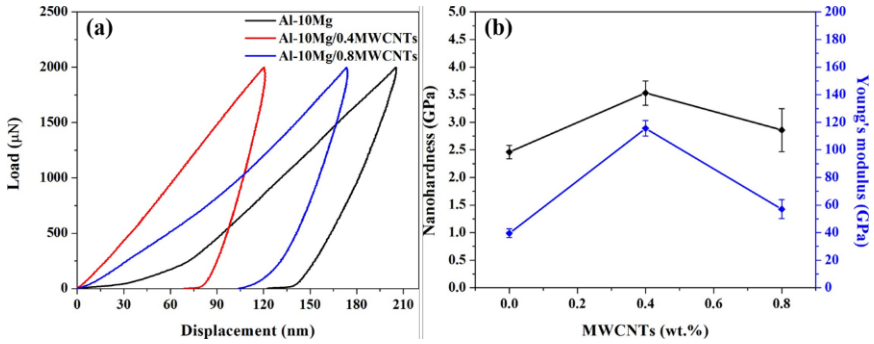

Fig. 7. Mechanical properties of the materials, Al-10Mg, Al-10Mg/0.4MWCNTs, and Al-10Mg/0.8MWCNTs. a) Load *vs.* displacement and b) nanohardness and Young's modulus.

4. Conclusion

In summary, the MWCNTs were purified, dispersed, and used as a reinforcing phase (0.4 wt.% and 0.8 wt.%) in the Al-10Mg alloy. An effective acid treatment was performed on the MWCNTs using HCl and HNO_3 showed a significant reduction in the FeNPs catalyst (80 wt.%) and the amorphous carbon. The E7E causes a good dispersion of MWCNTs at a concentration of 0.5 mg/ml. The Al-10Mg alloy shows good dispersion of MWCNTs after high-energy ball milling for 0.25 h. After the powders consolidation, the Al-10Mg/0.4MWCNTs nanocomposite shows a 91 % densification. The X-ray patterns showed the formation of the $MgAl_2O_4$ phase in the sintered samples. In the same way, the Al-10Mg/0.4MWCNTs nanocomposite presents the best values of microhardness (190 HV), nanohardness (3.5 GPa), and Young's modulus (116 GPa). These values are relatively higher than other Al-Mg-based matrix nanocomposites with similar compositions, which offers the possibility of their structural applications.

Acknowledgments

The authors are grateful for the financial support from Consejo Nacional de Ciencia y Tecnología (CONACYT).

5. References

1. H. Nie, M. Schoenitz, E.L. DREIZIN. Oxidation of differently prepared Al-Mg alloy powders in oxygen. J. Alloys Compd. 685 (2016), 402-410.
2. M. Alipour, R. Eslami-Farsani. Synthesis and characterization of graphene nanoplatelets reinforced AA7068 matrix nanocomposites produced by liquid metallurgy route. Mater. Sci. Eng. A. 706 (2017), 71-82.
3. V. Paradiso, F. Rubino, P. Carlone, G.S. Palazzo. Magnesium and aluminium alloys dissimilar joining by friction stir welding. Procedia Eng. 183 (2017), 239-244.
4. Y. Chi, G. Gu, H. Yu, C. Chen. Laser surface alloying on aluminum and its alloys: A review. Opt. Lasers Eng. 100 (2018), 23-37.
5. D.K. Koli, G. Agnihotri, R. Purohit. Advanced aluminium matrix composites: The critical need of automotive and aerospace engineering fields. Mater Today: Proc. 2 (2015), 3032-3041.
6. R. Purohit, M.M.U. Qureshi, B. Kumar. Effect of forging on aluminum matrix nano composites: A review. Mater Today: Proc. 4 (2017), 5357-5360.
7. A. Contreras, E. Bedolla, M. Salazar, J. Lemus. Metal Matrix Composites Wetting and Infiltration. First ed. Springer. 2018.
8. A. Sharma, H. Fujii, J. Paul. Influence of reinforcement incorporation approach on mechanical and tribological properties of AA6061-CNT nanocomposite fabricated via FSP. J. Manuf Processes. 59 (2020), 604-620.
9. N. Saheb, M. Shahzeb. Compressive strength and thermal properties of spark plasma sintered Al-Al_2O_3 nanocomposite. Sci. Sintering. 50 (2018), 1-14.
10. B. Singh, S. Chandel, P. Singhal. Investigation of mechanical properties of synthesized AA2024-T351/SiO_2 metal matrix nano-composite. Mater Today: Proc. 26 (2020), 1082-1086.
11. H. Durmuş, C. Gül, N. Çömez, R. Uzun. From Metal Chips to Composite: Effect of Age-Hardening on mechanical and wear properties of Al_2O_3 reinforced AA7075 composites. Sci. Sintering. 52 (2020), 177-186.
12. S.F. Hassan, M. Gupta. Development of nano-Y_2O_3 containing magnesium nanocomposites using solidification processing. J. Alloys Compd. 429 (2007), 176-183.
13. S.B. Boppana, S. Dayanand, M.R. Anil Kumar, V. Kumar, T. Aravinda. Synthesis and characterization of nano graphene and ZrO_2 reinforced Al 6061 metal matrix composites. J. Mater Res Technol. 9 (2020), 7354-7362.
14. H. Yang, T. Gao, Y. Wu, H. Zhang, J. Nie, X. Liu. Microstructure and mechanical properties at both room and high temperature of in-situ TiC reinforced Al-4.5Cu matrix nanocomposite. J. Alloys Compd. 767 (2018), 606-616.
15. M. Pul. Effect of B_4C reinforcement ratio and sintering temperature on the mechanical behavior in Al-B_4C composites. Sci. Sintering. 50 (2018), 51-61.
16. D. Luo, C.H. Pei, J. Rong, H.Y. Wang, Q. Li, Q.C. Jiang. Microstructure and mechanical properties of SiC particles reinforced Mg-8Al-1Sn magnesium matrix composites fabricated by powder metallurgy. Powder Metall. 58 (2015), 349-353.
17. H. Fernández, S. Ordoñez, H. Pesenti, R. Espinoza González, M. Leoni. Microstructure homogeneity of milled aluminum A356-Si_3N_4 metal matrix composite powders. J. Mater Res Technol. 8 (2019), 2969-2977.

18. A. El-Ghazaly, G. Anis, H.G. Salem. Effect of graphene addition on the mechanical and tribological behavior of nanostructured AA2124 self-lubricating metal matrix composite. Compos Part A. 95 (2017), 325-336.
19. K. Choi, J. Seo, D. Bae, H. Choi. Mechanical properties of aluminum-based nanocomposite reinforced with fullerenes. Trans Nonferrous Met Soc China. 24 (2014), s47-s52.
20. F. Khodabakhshi, A.P. Gerlich, P. Švec. Reactive friction-stir processing of an Al-Mg alloy with introducing multi-walled carbon nano-tubes (MW-CNTs): Microstructural characteristics and mechanical properties. Mater Charact. 131 (2017), 359-373.
21. M.F.L. Volder, S.H. Tawfick, R.H. Baughman, A.J. Hart. Carbon nanotubes: Present and future commercial applications. Sci. 339 (2013), 535-539.
22. H. Dai. Carbon nanotubes: Opportunities and challenges. Surf Sci. 500 (2002), 218-241.
23. P.V. Trinh, N.V. Luan, D.D. Phuong, P.N. Minh. Mirostructure and microhardness of aluminum-copper composite reinforced with multi-walled carbon nanotubes prepared by vacuum sintering and hot isostatic pressing techniques. Sci. Sintering. 50 (2018), 163-171.
24. V. Sivamaran, V. Balasubramanian, M. Gopalakrishnan, V. Viswabaskaran, A. Gourav Rao, G. Sivakumar. Mechanical and tribological properties of Self-Lubricating Al 6061 hybrid nano metal matrix composites reinforced by nSiC and MWCNTs. Surf Interfaces. 21 (2020).
25. M. Darabi, M. Rajabi, B. Junipour, M.T. Noghani. The effect of sintering temperature on Cu-CNTs nano composites properties produced by PM method. Sci. Sintering. 50 (2018), 477-486.
26. J. Ružić, M. Simić, N. Stoimenov, D. Božić, J. Stašić. Innovative processing routes in manufacturing of metal matrix composite materials. Metall. Mater. Eng. 27 (2021), 1-13.
27. C.A. Isaza Merino, J.E. Ledezma Sillas, J.M. Meza, J.M. Herrera Ramirez. Metal matrix composites reinforced with carbon nanotubes by an alternative technique. J. Alloys Compd. 707 (2017), 257-263.
28. H. Mindivan, A. Efe, A.H. Kosatepe, E.S. Kayali. Fabrication and characterization of carbon nanotube reinforced magnesium matrix composites. Appl Surf Sci. 318 (2014), 234-243.
29. G. Liu, N. Zhao, C. Shi, E. Liu, F. He, L. Ma, Q. Li, J. Li, C. He. In-situ synthesis of graphene decorated with nickel nanoparticles for fabricating reinforced 6061Al matrix composites. Mater. Sci. Eng. A. 699 (2017), 185-193.
30. J. Liang, H. Li, L. Qi, W. Tian, X. Li, X. Chao, J. Wei. Fabrication and mechanical properties of CNTs/Mg composites prepared by combining friction stir processing and ultrasonic assisted extrusion. J. Alloys Compd. 728 (2017), 282-288.
31. D. Mendoza-Cachú, C. Mercado-Zúñiga, G. Rosas. Surfactant assisted stabilization of carbon nanotubes synthesized by a spray pyrolysis method. Adv Condens Matter Phys. 1 (2017), 1-7.
32. J.J. Sánchez-Cuevas, J. Zárate-Medina, O. Navarro, C. Mercado-Zúñiga, F.J. Reynoso-Marín, G. Rosas. Microstructure and microhardness of the Al-10Mg alloy processed by the mechanical alloying technique. Sci. Sintering. 52 (2020), 123-133.
33. S. Simões, F. Viana, M.A.L. Reis, M.F. Vieira. Improved dispersion of carbon nanotubes in aluminum nanocomposites. Compos Struct. 108 (2014), 992-1000.
34. W.C. Oliver, G.M. Pharr. An improved technique for determining hardness and elastic modulus using load and displacement sensing indentation experiments. J. Mater Res. 7 (1992), 1564-1583.
35. A.C. Fischer-Cripps. Nanoindentation. Second ed. Springer. 2004.

36. K. Ghosh, M. Kumar, T. Maruyama, Y. Ando. Micro-structural, electron-spectroscopic and field-emission studies of carbon nitride nanotubes grown from cage-like and linear carbon sources. Carbon. 47 (2009), 1565-1575.
37. R.A. Afre, T. Soga, T. Jimbo, M. Kumar, Y. Ando, M. Sharon, P.R. Somani, M. Umeno. Carbon nanotubes by spray pyrolysis of turpentine oil at different temperatures and their studies. Microporous Mesoporous Mater. 96 (2006), 184-190.
38. L. Stobinski, B. Lesiak, L. Kövér, J. Tóth, S. Biniak, G. Trykowski, J. Judek. Multiwall carbon nanotubes purification and oxidation by nitric acid studied by the FTIR and electron spectroscopy methods. J. Alloys Compd. 501 (2010), 77-84.
39. B. Scheibe, E. Borowiak-Palen, R.J. Kalenczuk. Oxidation and reduction of multiwalled carbon nanotubes-preparation and characterization. Mater Charact. 61 (2010), 185-191.
40. F. Zhao, H. Duan, W. Wang, J. Wang. Synthesis and characterization of magnetic Fe/CNTs composites with controllable Fe nanoparticle concentration. Physica B. 407 (2012), 2495-2499.
41. M. Ghazanfari, A. Yazdani. Influence of MWCNTs on the formation, structure and magnetic properties of magnetite. Mater Sci Semicond Process. 40 (2015), 152-157.
42. R.A. Jishi, L. Venkataraman, M.S. Dresselhaus, G. Dresselhaus. Phonon modes in carbon nanotubules. Chem Phys Lett. 209 (1993), 77-82.
43. L. Vaisman, H.D. Wagner, G. Marom. The role of surfactants in dispersion of carbon nanotubes. Adv Colloid Interface Sci. 128-130 (2006), 37-46.
44. X. Ling, Y. Wei, L. Zou, S. Xu. Functionalization and dispersion of multiwalled carbon nanotubes modified with poly-l-lysine. Colloids Surf, A. 443 (2014), 19-26.
45. C.N. He, N.Q. Zhao, C.S. Shi, S.Z. Song. Mechanical properties and microstructures of carbon nanotube-reinforced Al matrix composite fabricated by in situ chemical vapor deposition. J. Alloys Compd. 487 (2009), 258-262.
46. Q. Li, A. Viereckl, C.A. Rottmair, R.F. Singer. Improved processing of carbon nanotube/magnesium alloy composites. Compos Sci Technol. 69 (2009), 1193-1199.
47. A. Maqbool, M.A. Hussain, F.A. Khalid, N. Bakhsh, A. Hussain, M.H. Kim. Mechanical characterization of copper coated carbon nanotubes reinforced aluminum matrix composites. Mater Charact. 86 (2013), 39-48.
48. H.T. Li, Y. Wang, Z. Fan. Mechanisms of enhanced heterogeneous nucleation during solidification in binary Al-Mg alloys. Acta Mater. 60 (2012), 1528-1537.
49. D. Singh, C. Suryanarayana, L. Mertus, R.H. Chen. Extended homogeneity range of intermetallic phases in mechanically alloyed Mg-Al alloys. Intermetallics. 11 (2003), 373-376.
50. R. Zhao, R. Xu, G. Fan, K. Chen, Z. Tan, D.B. Xiong, Z. Li, S.D. Kaloshkin, D. Zhang. Reinforcement with in-situ synthesized carbon nano-onions in aluminum composites fabricated by flake powder metallurgy. J. Alloys Compd. 650 (2015), 217-223.
51. J. Zhang, G. Luo, Y. Wang, Q. Shen, L. Zhang. An investigation on diffusion bonding of aluminum and magnesium using a Ni interlayer. Mater Lett. 83 (2012), 189-191.
52. C.R. Bradbury, J.K. Gomon, L. Kollo, H. Kwon, M. Leparoux. Hardness of multi wall carbon nanotubes reinforced aluminium matrix composites. J. Alloys Compd. 585 (2014), 362-367.
53. M.H. Nai, J. Wei, M. Gupta. Interface tailoring to enhance mechanical properties of carbon nanotube reinforced magnesium composites. Mater Des. 60 (2014), 490-495.
54. M. Rashad, F. Pan, M. Asif. Room temperature mechanical properties of Mg-Cu-Al alloys synthesized using powder metallurgy method. Mater. Sci. Eng. A. 644 (2015), 129-136.

55. X. Zeng, G. Zhou, Q. Xu, Y. Xiong, C. Luo, J. Wu. A new technique for dispersion of carbon nanotube in a metal melt. Mater. Sci. Eng. A. 527 (2010), 5335-5340.
56. M. Paramsothy, X.H. Tan, J. Chan, R. Kwok, M. Gupta. Carbon nanotube addition to concentrated magnesium alloy AZ81: Enhanced ductility with occasional significant increase in strength. Mater Des. 45 (2013), 15-23.
57. K. Kondoh, H. Fukuda, J. Umeda, H. Imai, B. Fugetsu, M. Endo. Microstructural and mechanical analysis of carbon nanotube reinforced magnesium alloy powder composites. Mater. Sci. Eng. A. 527 (2010), 4103-4108.

Сажетак: *У овом раду, карбонске нанотубе са мноштвом зидова (MWCNTs) су пречишћене киселином и дисперговане ултразвуком и сурфактантом на бази етилен оксида (E7E). Затим су карбонске нанотубе (CNTs) употребљене као ојачање (0.4 wt.% и 0.8 wt.%) у Al-10Mg легури. Нанокомпозити су процесуирану у високо-енергетском планетарном млину а након тога униаксијално пресовани. На чврстим узорцима су изведена мерења тврдоће по Викерсу, наночврстоће, и Јунговог модула еластичности. Узорци су анализирани методама као што су SEM, XRD, UV-Vis, FT-IR, и Раман спектроскопија. Добра дисперзија MWCNTs је постигнута употребом 0.5 mg/ml E7E сурфактанта. CNTs су дисперговане у Al-10Mg матриксу након 0.25 h млевења. Након компактирања прахова, Al-10Mg/0.4MWCNTs нанокомпозит је имао микрочврстоћу од 190 HV, нанотврдоћу 3.5 GPa, и Јунгов модул еластичности 116 GPa.*
Кључне речи: *Al-10Mg/MWCNTs нанокомпозити, високо-енергетско млевење; микротврдоћа; наночврстоћа; Јунгов модул.*